RESEARCH ARTICLE

An optimization-based phase-field method for continuous-discontinuous crack propagation

Rudy J.M. Geelen[1] | Yingjie Liu[2] | John E. Dolbow[1,2] | Antonio Rodríguez-Ferran[3]

[1]Department of Mechanical Engineering and Materials Science, Duke University, Durham, NC 27708, USA
[2]Department of Civil and Environmental Engineering, Duke University, Durham, NC 27708, USA
[3]Laboratori de Càlcul Numèric (LaCàN), Universitat Politècnica de Catalunya, BarcelonaTech, 08034 Barcelona, Spain

Correspondence
John Dolbow, Email: jdolbow@duke.edu

Abstract

A new continuous-discontinuous strategy for the computational modeling of crack propagation within the context of phase-field models of fracture is presented. The method is designed to introduce and update a sharp crack surface within an evolving damage band, and to enhance the kinematics of the finite element approximation accordingly. The proposed approach relies on three key elements. First, we propose the use of a crack length functional to provide a trigger for initiating a continuous to discontinuous transition. Next, the crack path identification is addressed by introducing the concept of an auxiliary damage field that varies with an extension of the sharp crack surface. The sharp crack surface is extended through an optimization algorithm, in which the difference between the auxiliary field and the actual damage field stemming from the phase-field framework is minimized. Finally, a strong discontinuity is inserted in the wake of the diffuse crack tip with the eXtended Finite Element Method (X-FEM), completing the continuous to discontinuous transition. Several benchmark problems in two-dimensional quasi-static fracture mechanics are presented to demonstrate the accuracy and robustness of the method.

KEYWORDS:
phase-field approach; X-FEM; crack propagation; optimization; finite elements

1 | INTRODUCTION

Gradient-damage models of fracture have become increasingly popular over the past decade in no small part due to their potential for capturing the evolution of complex fracture patterns. This includes recent work on phase-field models of fracture[1–4], as well as the Thick Level Set (TLS) method[5], among others. With the exception of the TLS, methods based on gradient-damage models do not provide a means to identify a distinct crack surface within a fully damaged band. The lack of a distinct crack surface can be problematic for a number of reasons, ranging from difficulties imposing crack-surface physics to mesh distortion and poor conditioning. This work builds on recent efforts to employ optimization algorithms[6] in the identification process, by developing a methodology that works well for propagating cracks and that can leverage the enhanced kinematics afforded by X-FEM enrichment. In this manner, the current approach primarily relies on the continuum damage representation to govern the evolution of the crack geometry, circumventing challenges for sharp crack representations around crack nucleation, branching, and coalescence. The optimization process and accompanying X-FEM enrichment follows in the wake of the geometric evolution as a means to transition from the continuum damage representation to sharp fracture surfaces, as suggested by Sukumar *et al.*[7].

Over the past decade, a great deal of attention has been placed on the use of phase-field regularizations of fracture for simulations of brittle crack growth. Pioneering work in this area was performed by Ambrosio and Tortorelli[8], who introduced a

phase-field approximation to the potential presented by Mumford and Shah[9] using elliptic functionals. The same approximation was used by Bourdin and co-workers[2] to develop a variational framework based on Griffith's theory of brittle fracture. More recently, an alternative derivation was proposed from thermodynamical considerations by Miehe *et al.*[3,4] This formulation broadened the scope of phase-field modeling by introducing viscous effects, an anisotropic energy storage function, and a local history field to address irreversibility. In addition, it is consistent with classical continuum-damage literature, given that the phase-field can be interpreted as a damage variable. A comparison between gradient-damage and phase-field models of fracture is provided in de Borst and Verhoosel.[10]

As a fracture problem evolves, both phase-field and gradient-damage approaches give rise to fully damaged regions that approximate a sharp crack geometry. In a standard finite element discretization, the width of such "damage bands" can easily exceed the mesh spacing. The result can be large regions of the computational domain that are fully damaged and that effectively exhibit zero stiffness. These regions introduce several issues for the methods that are challenging to address in a robust manner. For example, many implementations employ a small stabilization parameter that prevents a complete loss of stiffness at full damage. Importantly, such approaches do give rise to the spurious transmission of tractions across the damage band. It can be difficult to identify a parameter that is large enough to circumvent conditioning problems but not so large as to adversely affect the results. Another issue that arises for simulations with large strains concerns the possibility of significant mesh distortion in regions of full damage. Finally, we mention that in many problems having an explicit crack surface is desirable from the standpoint of easily incorporating additional physics.

To a large extent, the aforementioned issues are reflective of the inherent limitations of a strict damage point of view for modeling the fracture process. In reality a damaged region eventually becomes a fracture surface that is traction-free, and what is required is a transition from damage to fracture. This basic issue has been a topic of study for some time, dating back to early work by Mazars and Pijaudier-Cabot.[11] In that work, relationships based on thermodynamic considerations between the two theories were presented. By transitioning from a damage zone to a fracture problem, and vice versa, a damage zone was determined that is equivalent to a crack. In Oliver *et al.*[12] the strong discontinuity approach was presented. A regularized kinematic state of a discontinuity was proposed as a means to model the formation of a strong discontinuity as the collapsed state of a weak discontinuity. While the original model was proposed in the context of continuum plasticity models, it has been extended to continuum damage models in infinitesimal[13] and finite strain settings[14]. In Jirasek *et al.*[15] a strategy was outlined to transition from a smeared to an embedded crack representation. The basic idea was to define a critical damage value beyond which a continuous-discontinuous transition is triggered, after which an energetically equivalent cohesive crack is inserted. Similar strategies have been employed in the context of gradient-enhanced damage models [16–18] and gradient-enhanced coupled damage-plasticity models[19].

In addition to the aforementioned works, some researchers have adopted different perspectives to introduce distinct crack surfaces within fully damaged bands. One way of coping with the difficulties of a continuous to discontinuous transition is through the use of post-processing techniques. Dufour *et al.*[20,21] used a damage model to characterize the fracture process, where the crack path and crack tip opening displacement are computed in a post-processing step. Another strategy can be found in the Thick Level Set (TLS) approach.[5] The TLS attempts to address some of the issues associated with the transition from damage to fracture through the use of a level set function that separates the undamaged material from the damaged material. Hence, crack growth is expressed as a propagating level set. Beyond a critical length, the material is assumed to be fully damaged, and the finite element approximation is enriched through the extended finite element method (X-FEM). This permits the method to capture true displacement discontinuities within fully damaged elements.

More recently, Tamayo-Mas and Rodríguez-Ferran[22] proposed an integrated continuous-discontinuous strategy based on the medial-axis algorithm. This geometrical approach intuitively places a crack through the middle of the damage band in a regularized bulk. As soon as the damage parameter is close to unity, a traction-free crack is introduced. Wang and Waisman[23] outlined an integrated continuous-discontinuous approach based on the coupling of an integral-type non-local continuum damage model to a sharp cohesive interface model using X-FEM. Special attention was given to the transition from damage to cohesive cracks through an equivalent thermodynamic framework established in a multidimensional setting. In Ziaei-Rad *et al.*[6] a method was presented to identify the crack path using a damage field that stems from a variational formulation. The underlying algorithm employs the non-maximum suppression technique, a procedure borrowed from the image processing community. However, the study was restricted to stationary cracks. Finally, in Giovanardi *et al.*[24], a novel method was presented in which a large scale displacement solution was obtained with the extended finite element method, while the propagation was governed by the solution of a local phase-field problem at the crack tip. The proposed approach was successfully applied to crack propagation problems, but has yet to demonstrate robustness when accounting for branching and merging cracks.

In this work, we develop a new approach for continuous to discontinuous transitions for simulations of brittle fracture. While the approach is based on a phase-field model of fracture, in principle the basic aspects could be applied to gradient-damage models as well. The method relies on energetic considerations that capture changes to the regularized crack length as a means to trigger the transition process. Distinct crack surfaces are identified within damage bands using an optimization approach that is similar to that described in Ziaei-Rad *et al.*[6] Finally, once new crack surfaces are determined, the method enriches the finite element approximation such that strong discontinuities can be captured. We note that many phase-field and continuum damage approaches rely on some form of numerical regularization to prevent a loss of ellipticity from occurring due to fully-damaged regions. Importantly, the current approach circumvents the need for this kind of stabilization.

The remainder of this paper is organized as follows. In Section 2 we introduce regularized crack topologies using a phase-field approximation. Next, the phase-field approach to brittle fracture is reviewed and the corresponding governing equations are presented. We demonstrate how a closed-form analytical solution to the one-dimensional quasi-static problem leads to the auxiliary damage concept, which is used to approximate the damage field stemming from the phase-field framework. Section 3 introduces the numerical formulation of the variational problem. The weak form of the coupled problem is formulated by means of the Galerkin method and is completed by a spatial discretization for the continuous-discontinuous modeling of crack propagation. In particular, the extended finite-element approximation and its implementation in the current method is described. Section 4 details a strategy for dealing with the transition from damage to fracture. This procedure involves addressing the following consecutive steps: (i) the definition of a switching criterion; (ii) the crack-path definition; and (iii) introducing an appropriate enhancement of the kinematics. A local optimization problem is defined for the handling of the continuous to discontinuous transition in which the auxiliary damage is a primary tool. In addition, a robust computational implementation is presented based on a staggered solution algorithm. Section 5 provides various numerical examples that demonstrate the versatility of the proposed method in handling crack initiation and propagation, as well as the merging and branching of cracks. Finally, a summary and some concluding remarks are provided in the last section.

2 | THE PHASE-FIELD APPROACH TO BRITTLE FRACTURE

In this work, two distinct representations of the crack geometry will be employed, which we refer to as the *diffuse* crack and the *sharp* crack. The evolution of the diffuse crack is governed by a phase-field method, which is described in the following two subsections. The evolution of the sharp crack makes use of an auxiliary damage field, as described in Section 2.3, and an optimization method, described in Section 4.

2.1 | The phase-field approximation

The basic idea behind the phase-field approximation to brittle fracture is the use of a diffuse crack functional Γ_l that smears a discontinuity Γ over a domain Ω

$$\Gamma_l(d) = \int_\Omega \gamma_l(d, \nabla d)\, d\mathbf{x} \tag{1}$$

where the crack surface density function per unit volume of the solid can be expressed as

$$\gamma_l(d, \nabla d) = \left(\frac{1}{2l} d^2 + \frac{l}{2} \nabla d \cdot \nabla d \right) \tag{2}$$

where l is the regularization length.[3] The crack surface density functional corresponds with terms obtained in Γ-convergent regularizations of free discontinuity problems by elliptic functionals outlined in the work from Ambrosio and Tortorelli.[8] This functional, which depends on the continuous field variable d, and its spatial gradient ∇d, plays a crucial role in the phase-field modeling of fracture. Following continuum damage mechanics conventions, the damage variable (also phase-field variable) $d \in [0, 1]$ is defined such that $d = 0$ characterizes an intact state of the material, while $d = 1$ represents fully broken material. We note that the crack surface density function in (2) carries dimensions of inverse length, such that when integrated over Ω the expression (1) for the diffuse crack functional Γ_l has dimensions of length (2D) or surface area (3D).

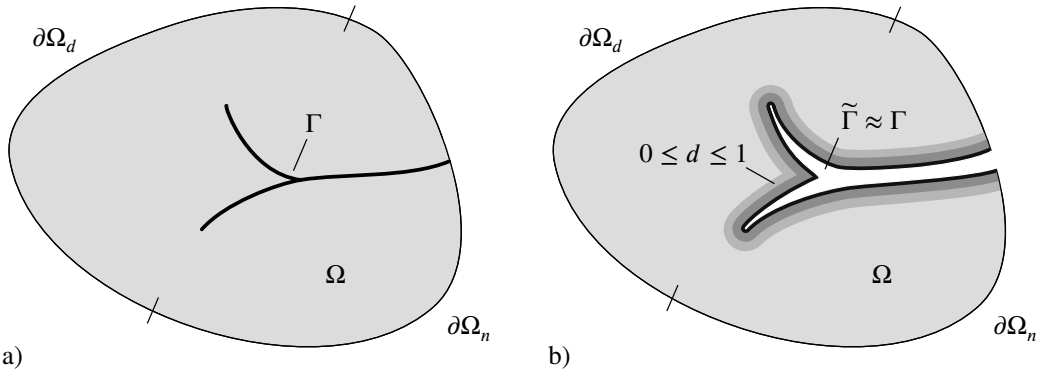

FIGURE 1 a) Sketch of a solid body, Ω, with an internal discontinuity Γ. b) A continuous-discontinuous representation of the internal discontinuity by means of a damage field $d(\mathbf{x}, t)$ and an approximate sharp discontinuity $\widetilde{\Gamma}$.

2.2 | Continuum formulation of the phase-field model

Consider an arbitrary body $\Omega \subset \mathbb{R}^{n_{sd}}$ and external boundary $\partial\Omega$ with internal discontinuity Γ (see Figure 1 a) where n_{sd} denotes the number of spatial dimensions. The displacement at an arbitrary point $\mathbf{x} \in \Omega$ at time $t \in [0, T]$ is denoted by $\mathbf{u}(\mathbf{x}, t) \in \mathbb{R}^{n_{sd}}$. The displacement field satisfies Dirichlet and Neumann boundary conditions on $\partial\Omega_d$ and $\partial\Omega_n$, respectively. The value of the phase-field variable is defined to be $d = 1$ on the fracture surface and $d = 0$ sufficiently far away from it (see Figure 1 b). Within this damage band, we identify a surface $\widetilde{\Gamma}$ that is meant to approximate the original crack surface Γ, in a manner to be described in Section 4.2. We assume small deformations and define the infinitesimal strain tensor, $\boldsymbol{\varepsilon}(\mathbf{x}, t) \in \mathbb{R}^{n_{sd} \times n_{sd}}$

$$\boldsymbol{\varepsilon}(\mathbf{u}) = \frac{1}{2}\left[\nabla\mathbf{u} + (\nabla\mathbf{u})^T\right] \tag{3}$$

as the deformation measure. We restrict ourselves to the theory of linear elasticity of isotropic solids. In that case the reference elastic energy density is given by

$$W_0 = \frac{1}{2}\lambda\,[\mathrm{Tr}\,\boldsymbol{\varepsilon}]^2 + \mu\,\boldsymbol{\varepsilon} : \boldsymbol{\varepsilon} \tag{4}$$

with λ and μ the Lamé constants. The elastic energy density describes the energy stored in the bulk of the solid per unit volume. We follow Miehe *et al.*[4] in defining an anisotropic energy storage function

$$W(\boldsymbol{\varepsilon}(\mathbf{u}), d) = g(d)W_0^+(\boldsymbol{\varepsilon}) + W_0^-(\boldsymbol{\varepsilon}) \tag{5}$$

This formulation is based on an additive decomposition of the reference elastic energy density of the undamaged solid into a positive part W_0^+ due to tension and a negative part W_0^- due to compression. In particular,

$$W_0^+(\boldsymbol{\varepsilon}) = \frac{1}{2}\lambda\,\langle\mathrm{Tr}\,\boldsymbol{\varepsilon}\rangle_+^2 + \mu\boldsymbol{\varepsilon}_+ : \boldsymbol{\varepsilon}_+ \quad \text{and} \quad W_0^-(\boldsymbol{\varepsilon}) = \frac{1}{2}\lambda\,\langle\mathrm{Tr}\,\boldsymbol{\varepsilon}\rangle_-^2 + \mu\,\boldsymbol{\varepsilon}_- : \boldsymbol{\varepsilon}_- \tag{6}$$

in terms of bracket operators $\langle x\rangle_+ := (x + |x|)/2$ and $\langle x\rangle_- := (x - |x|)/2$. Since the damage only degrades the tensile part of the elastic energy density, crack growth under compression is prohibited. The positive and negative parts of the strain follow from a spectral decomposition of the form:

$$\boldsymbol{\varepsilon}_\pm := \sum_{a=1}^{n_{sd}} \langle\varepsilon_a\rangle_\pm\,\mathbf{n}_a \otimes \mathbf{n}_a \tag{7}$$

where $\{\varepsilon_a\}_{a=1,\ldots,n_{sd}}$ are the principal strains and $\{\mathbf{n}_a\}_{a=1,\ldots,n_{sd}}$ the principal strain directions. For further details regarding this construction we refer to Miehe *et al.*[3] and the references therein.

In (5), the function $g(d)$ controls the degradation of the elastic energy density due to the evolution of damage. A commonly used degradation function is

$$g(d) = (1 - d)^2\,. \tag{8}$$

Following Griffith's theory of brittle fracture, the potential energy for a solid with crack surface Γ reads:

$$\Pi = \int_{\Omega} W(\boldsymbol{\varepsilon}(\mathbf{u}), d)\, d\mathbf{x} + \int_{\Gamma} \mathcal{G}_c\, d\mathbf{x} \tag{9}$$

where $\mathcal{G}_c$ denotes the critical fracture energy density. Phase-field models of fracture employ the crack surface density function (2) to approximate the surface integral, leading to

$$\Pi \approx \Pi_l = \int_{\Omega} W(\boldsymbol{\varepsilon}(\mathbf{u}), d)\, d\mathbf{x} + \int_{\Omega} \mathcal{G}_c \gamma_l(d, \nabla d)\, d\mathbf{x} \tag{10}$$

The irreversibility constraint $d(\cdot, t_1) \leq d(\cdot, t_2)$ for $t_1 \leq t_2$ is enforced by means of a local history field $\mathcal{H}(\mathbf{x}, t)$ that satisfies the Kuhn-Tucker conditions:

$$W_0^+ - \mathcal{H} \leq 0, \quad \dot{\mathcal{H}} \geq 0, \quad \dot{\mathcal{H}}(W_0^+ - \mathcal{H}) = 0 \tag{11}$$

Substituting $\mathcal{H}$ for W_0^+ and taking the Euler-Lagrange equations of (10) yields the strong form of the variational problem:

$$(S)\begin{cases} \text{Div}\,[\boldsymbol{\sigma}] = \mathbf{0} & \text{on } \Omega\times]0,T[\\ \dfrac{\mathcal{G}_c}{l}\left[d - l^2\Delta d\right] - 2(1-d)\mathcal{H} = 0 & \text{on } \Omega\times]0,T[\end{cases} \tag{12}$$

where the Cauchy stress tensor $\boldsymbol{\sigma} \in \mathbb{R}^{d\times d}$ is given by

$$\boldsymbol{\sigma} = g(d)\frac{\partial W_0^+}{\partial \boldsymbol{\varepsilon}} + \frac{\partial W_0^-}{\partial \boldsymbol{\varepsilon}}\,. \tag{13}$$

The system of equations is complemented by the boundary conditions

$$(S\,:\,BC)\begin{cases} \boldsymbol{\sigma}\cdot\mathbf{n} = \mathbf{t} & \text{on } \partial\Omega_n \\ \mathbf{u} = \bar{\mathbf{u}} & \text{on } \partial\Omega_d \\ \nabla d\cdot\mathbf{n} = 0 & \text{on } \partial\Omega \end{cases} \tag{14}$$

with $\partial\Omega_n \cap \partial\Omega_d = \emptyset$, $\partial\Omega_n \cup \partial\Omega_d = \partial\Omega$, prescribed tractions and displacements $\bar{\mathbf{t}}$ and $\bar{\mathbf{u}}$, respectively, and with $\mathbf{n}$ denoting the outward-pointing normal vector along the boundary.

2.3 | The auxiliary damage field

We now motivate the use of an expression for an auxiliary damage field that will be employed in an optimization framework to identify a sharp crack surface. The basic idea is to identify a field that is a function of a sharp crack surface geometry. We begin by examining the analytical solution for a particular boundary value problem in one dimension. We consider the domain $0 \leq x \leq \infty$ subjected to uniaxial tension and assume a monotonically increasing, non-negative strain field. Under these conditions, it can be shown that the damage field should satisfy the nonlinear ordinary differential equation[25]

$$\frac{\mathcal{G}_c}{l}\left[d - l^2\frac{\mathrm{d}^2 d}{\mathrm{d}x^2}\right] = \frac{\sigma^2}{(1-d)^3 E}\,. \tag{15}$$

We note that the nonlinearity stems from the dependence of the stress on the damage through (13). A solution for the damage field, with a sharp crack centered at $x = 0$, is found multiplying (15) with $\frac{\mathrm{d}d}{\mathrm{d}x}$ and making use of the fact that the stress is constant, to obtain

$$\frac{\mathrm{d}}{\mathrm{d}x}\left[\frac{\mathcal{G}_c d^2}{2l} - \frac{\sigma^2}{2E(1-d)^2} - \frac{1}{2}\left(\frac{\mathrm{d}d}{\mathrm{d}x}\right)^2 \mathcal{G}_c l\right] = 0\,. \tag{16}$$

For a fully developed crack, i.e. $\sigma = 0$, and by applying boundary conditions $d(0) = 1$ and $d(\infty) = 0$, we find

$$d(x) = \exp\left(-\frac{|x|}{l}\right) \tag{17}$$

as the solution that satisfies the specified boundary conditions. This expression can be extended to a multidimensional setting in a straightforward manner, describing the notion of an *auxiliary damage field*[6]. This concept allows us to construct an auxiliary

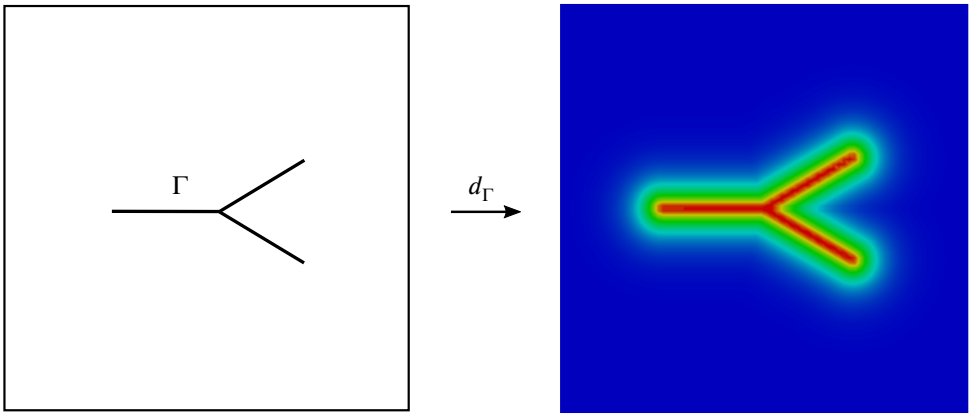

FIGURE 2 An arbitrary branched crack as a sharp crack topology (left) and the corresponding diffuse representation using an auxiliary damage field from (18) (right).

damage field for an arbitrary sharp crack surface Γ by means of the analytical expression

$$d_\Gamma(\mathbf{x},\Gamma) : \mathbf{x} \mapsto \exp\left(-\frac{\text{dist}(\mathbf{x},\Gamma)}{l}\right) \tag{18}$$

where $\text{dist}(\mathbf{x},\Gamma) := \inf_{\mathbf{x}^*\in\Gamma} |\mathbf{x}-\mathbf{x}^*|$ is the minimal distance from $\mathbf{x}$ to Γ. An auxiliary damage field for an arbitrary branched sharp crack topology is given in Figure 2 .

One issue with existing phase-field descriptions of fracture is the widening of the regularized fracture surface upon localization. To construct an auxiliary damage field that is expected to be a better match with the damage field stemming from the phase-field framework (12), we scale the auxiliary damage field as

$$d_\Gamma(\mathbf{x},\Gamma) : \mathbf{x} \mapsto \exp\left(-\frac{\text{dist}(\mathbf{x},\Gamma)}{s\cdot l}\right) \tag{19}$$

where $s \geq 1$ is a constant scaling parameter. The precise value of s used by the current method will be detailed in Section 5.

3 | NUMERICAL FORMULATION

3.1 | Weak form and Galerkin approximation

To compute an approximate solution to the strong form (12) using a finite element method, the weak form is derived. The discrete equations are constructed by the standard Galerkin procedures. We define the admissible function spaces $\mathcal{U}$ for the displacements and $\widetilde{\mathcal{U}}$ for the damage fields as follows:

$$\mathcal{U} = \left\{\mathbf{u}(\mathbf{x},t) \in \mathcal{V} \mid \mathbf{u} = \bar{\mathbf{u}} \text{ on } \partial\Omega_d\right\} \tag{20}$$

$$\widetilde{\mathcal{U}} = \{d(\mathbf{x},t) \in \mathcal{V}\} \tag{21}$$

where space $\mathcal{V}$ is connected to the regularity of the solution and is detailed in Babuška and Rosenzweig[26] and Grisvard[27]. This function space contains discontinuous fields of the displacements and damage across the sharp crack surfaces. Similarly the weighting function spaces are defined as

$$\mathcal{U}_0 = \left\{\delta\mathbf{u}(\mathbf{x},t) \in \mathcal{V} \mid \delta\mathbf{u} = \mathbf{0} \text{ on } \partial\Omega_d\right\} \tag{22}$$

$$\widetilde{\mathcal{U}}_0 = \{\delta d(\mathbf{x},t) \in \mathcal{V}\} \tag{23}$$

Multiplying (12) with the appropriate admissible solution and integrating by parts leads to the weak formulation

$$(\mathcal{W})\begin{cases} \text{Given } \bar{\mathbf{u}}, \bar{\mathbf{t}}, \text{ find } \mathbf{u}(\mathbf{x},t) \in \mathcal{U} \text{ and } d(\mathbf{x},t) \in \widetilde{\mathcal{U}} \text{ such that for all } \delta\mathbf{u} \in \mathcal{U}_0 \text{ and for all } \delta d \in \widetilde{\mathcal{U}}_0 \\ \qquad (\boldsymbol{\sigma}, \nabla\delta\mathbf{u})_\Omega = (\bar{\mathbf{t}}, \delta\mathbf{u})_{\partial\Omega_n} \\ \left(\left(\dfrac{\mathcal{G}_c}{l} + 2\mathcal{H}\right) d, \delta d\right)_\Omega + \left(\mathcal{G}_c l \nabla d, \nabla\delta d\right)_\Omega = (2\mathcal{H}, \delta d)_\Omega \end{cases} \tag{24}$$

In the Galerkin method we let $\mathcal{U}^h \subset \mathcal{U}$, $\widetilde{\mathcal{U}}^h \subset \widetilde{\mathcal{U}}$, $\mathcal{U}_0^h \subset \mathcal{U}_0$ and $\widetilde{\mathcal{U}}_0^h \subset \widetilde{\mathcal{U}}_0$ be the usual finite-dimensional approximations to the function spaces of the weak form. This yields the Galerkin approximation

$$(\mathcal{G})\begin{cases} \text{Given } \bar{\mathbf{u}}, \bar{\mathbf{t}}, \text{ find } \mathbf{u}^h(\mathbf{x},t) \in \mathcal{U}^h \text{ and } d^h(\mathbf{x},t) \in \widetilde{\mathcal{U}}^h \text{ such that for all } \delta\mathbf{u}^h \in \mathcal{U}_0^h \text{ and for all } \delta d^h \in \widetilde{\mathcal{U}}_0^h \\ \qquad (\boldsymbol{\sigma}, \nabla\delta\mathbf{u}^h)_\Omega = (\bar{\mathbf{t}}, \delta\mathbf{u}^h)_{\partial\Omega_n} \\ \left(\left(\dfrac{\mathcal{G}_c}{l} + 2\mathcal{H}\right) d^h, \delta d^h\right)_\Omega + \left(\mathcal{G}_c l \nabla d^h, \nabla\delta d^h\right)_\Omega = \left(2\mathcal{H}, \delta d^h\right)_\Omega \end{cases} \tag{25}$$

We assume that the approximations to the displacement and damage fields are based in part on basis functions associated with a finite element mesh. We note that in the phase-field literature it is common to introduce a small regularization parameter $\eta \approx 0$ that provides a lower bound on the tensile stiffness as the damage $d \to 1$.[3,4] As such, the expression for the stress field (13) is modified as:

$$\boldsymbol{\sigma} = [g(d) + \eta] \frac{\partial W_0^+}{\partial \boldsymbol{\varepsilon}} + \frac{\partial W_0^-}{\partial \boldsymbol{\varepsilon}} \,. \tag{26}$$

This is a form of numerical regularization that endows completely damaged elements with a small degree of stiffness as a means to circumvent a loss of ellipticity in the discrete equations as a damage band widens. In the proposed method, we will find the use of such a parameter to be unnecessary due to the enhanced kinematics provided by the X-FEM enrichment, as described in the next section.

3.2 | Extended finite element approximation using a material regions approach

In the current approach, we approximate the displacement and damage fields using a particular version of the extended finite element method (X-FEM) proposed in Moës *et al.*[28] The method provides a means to introduce discontinuities across surfaces whose geometry is independent of the underlying finite element mesh. In the current method, the displacement is enriched with discontinuous functions in order to properly capture a jump in the field in the wake of a *diffuse* crack tip.

As a starting point, we consider approximations to the displacement and damage fields of the form

$$\mathbf{u}^h(\mathbf{x}) = \sum_{i \in \mathbb{I}} N_i(\mathbf{x}) \mathbf{u}_i + \sum_{j \in \mathbb{J} \subseteq \mathbb{I}} N_j(\mathbf{x}) H(\mathbf{x}) \mathbf{a}_j \tag{27}$$

$$d^h(\mathbf{x}) = \sum_{i \in \mathbb{I}} N_i(\mathbf{x}) d_i + \sum_{j \in \mathbb{J} \subseteq \mathbb{I}} N_j(\mathbf{x}) H(\mathbf{x}) c_j \tag{28}$$

where $\mathbb{I} = \{1, 2, ..., n_{\text{nod}}\}$ is a nodal index set (with n_{nod} the number of nodes in the mesh) and $\mathbb{J}$ is an index set of nodes whose basis functions are cut by a discontinuity Γ, respectively. In the above, $N_i(\mathbf{x})$ are the classical finite element shape functions and $H(\mathbf{x})$ is a generalized Heaviside function with respect to the sharp crack surface. Finally, $\{\mathbf{u}_i, \mathbf{a}_j\}$ and $\{d_i, c_j\}$ are the unknown coefficients associated with the standard finite element and discontinuous basis functions for the displacement and damage fields, respectively.

Such approximations (27) and (28) effectively permit jumps in the fields across surfaces that are not aligned with the finite element mesh. For geometrically complex fracture patterns, however, the use of standard Heaviside enrichment can be both cumbersome to implement and inadequate for capturing all of the kinematics. For example, if tip splitting or merging of the sharp crack is expected, then additional "junction" type enrichment functions are required and the bookkeeping can quickly become a challenge.

Accordingly, in this work we adopt the material regions approach recently proposed by Richardson *et al.*[29] for constructing enriched approximations for embedded, geometrically complex crack structures. Given the geometry Γ of a sharp crack superimposed on a background mesh, the method builds a new finite element approximation that has the proper kinematics across the sharp crack surfaces, including in the vicinity of branches. In the first step of the algorithm, every element in the mesh is

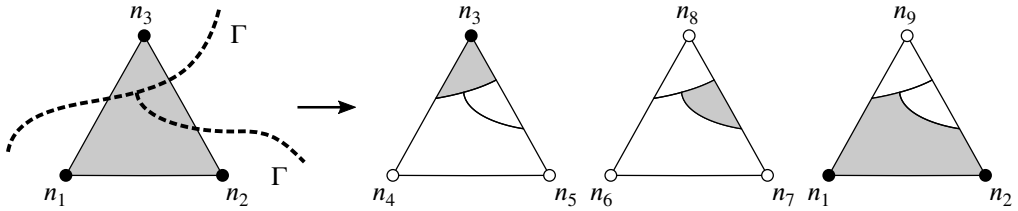

FIGURE 3 Cutting of a triangular element by a sharp crack network Γ. Left: the original triangular element. Right: partial elements associated with the different material regions. The regular nodes and virtual nodes are indicated by the solid and hollow circles, respectively.

considered individually. Consider for example the element shown in Figure 3 that contains two sharp crack surfaces that intersect on the interior of the element. The algorithm first creates three copies of this element as shown on the right in Figure 3 , one for each distinct material region formed by the sharp crack geometry. The three copies are referred to as *partial elements*, because they contain a material region that only occupies some portion of the element geometry. The produced set of partial elements is characterized by the three original nodes, n_1, n_2 and n_3, associated with the different material regions, and is complemented by a set of *virtual* nodes (nodes $n_4 - n_9$ depicted by the hollow circles). The second part of the algorithm resolves the global material connectivity by merging nodes (both real and virtual) between these elements and copies created by the first step of the algorithm applied to neighboring elements. Let us consider every partial element e^* of a given *parent* element e. For each element that neighbors e we evaluate whether one of its partial elements shares a *material connection* with e^*. If so, the nodes of the connected element edge are identified and the degrees of freedom on that edge are condensed into one unique set. The complete cutting algorithm given an arbitrary sharp crack network Γ for a triangulated domain is summarized in Figure 4 . Additional details regarding this approach are provided in Richardson *et al.*[29].

For a given sharp crack network that is represented by a series of connected segments in two dimensions, we use this material regions approach to build enriched approximations for both the displacement and damage fields. We note that, both from the modeling and physical point of view, it is not necessary to enrich the damage field with discontinuous functions. The shape of the damage profile from (17) is continuous across $\widetilde{\Gamma}$ but discontinuous in its derivative. Hence, it suffices to introduce a weak discontinuity in the damage field. However, the choice for discontinuous enrichment for both the displacement and the damage fields permits the use of the same infrastructure, simplifying the computational implementation. In addition, Heaviside enrichment can also be used to capture weak discontinuities as it enables two distinct linear fields to be represented on either side of a surface of discontinuity. We also point out that the enrichment of the damage field effectively introduces a new Neumann boundary on which a zero-flux condition is imposed. This is consistent with the expectation of a damage band about the sharp crack surface where $\nabla d \cdot \mathbf{n} \approx 0$.

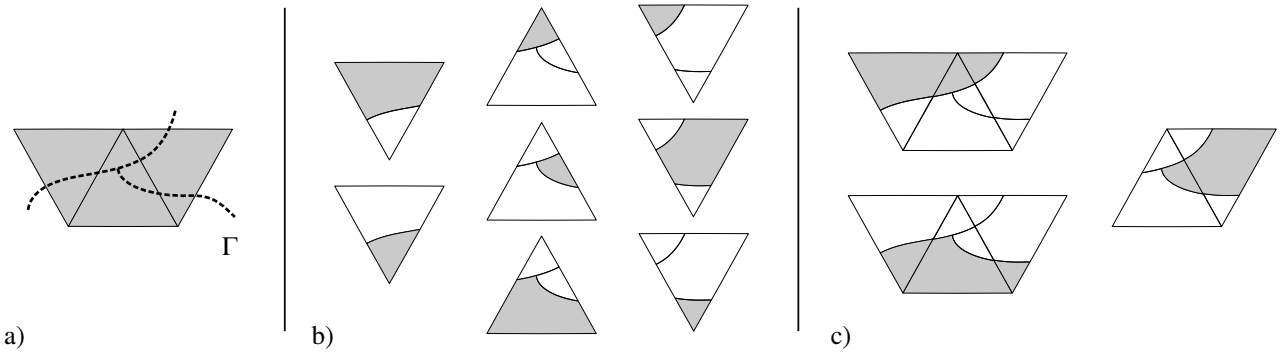

FIGURE 4 The consecutive steps in the material regions approach. a) Consider a triangulated domain cut by a sharp crack network Γ. b) Partial elements for each of the material regions in an element. c) Collapsing the degrees of freedom based on material connectivity along the element edges. We note that partial elements are represented by both a physical (shaded area) and a virtual part (blank area).

Finally, we note that approximations of this form do not permit sharp cracks to terminate at an arbitrary location within an element. Rather, sharp cracks must terminate at an element edge. In the current approach, this is viewed as somewhat less problematic than in other instances, as the enrichment follows in the *wake* of the diffuse crack.

4 | AN INTEGRATED APPROACH TO CONTINUOUS-DISCONTINUOUS FRACTURE

We follow Tamayo-Mas and Rodríguez-Ferran[22] in distinguishing three consecutive steps for a continuous to discontinuous transition. First but not foremost, we note that the definition of a *switching criterion* is instrumental in such a transition. Sharp crack surfaces that advance too quickly in the wake of a diffuse crack are at risk of failing material that has not yet fully degraded. Conversely, sharp crack surfaces that do not advance at an appropriate rate are characterized by regions where completely degraded elements may persist. Secondly, few studies have addressed the problem of *sharp crack-path definition* in a regularized bulk and, in fact, the crack trajectory is often assumed to be known beforehand. In this paper we analyze this geometrical problem through an optimization-based approach. The final step concerns the application of a cohesive law on the newly formed sharp crack surfaces, as a means to ensure that the energy transfer from the continuous to discontinuous state proceeds smoothly. In the present method, we will not impose any cohesive law on the sharp crack surfaces, and instead assume that all distinct sharp crack segments are traction-free. As such, only the switching criterion and the crack path definition are discussed in this section.

In our approach, sharp cracks are discretized by a series of connected, linear segments. With such a construction in two dimensions, one can easily identify the interior and any crack tips for an existing sharp crack. Sharp crack tips are located at an endpoint of the series of connected segments, with the exception of endpoints located at the boundary of the domain. The diffuse cracks whose evolution is described by the phase-field may also be viewed as having *diffuse crack tips*, but in our approach these do not need to be determined precisely.

4.1 | Switching criterion

We begin by considering the discrete *crack surface functional*

$$\Gamma_l(d^h) = \int_\Omega \left(\frac{1}{2l}(d^h)^2 + \frac{l}{2}\nabla d^h \cdot \nabla d^h \right) d\mathbf{x} \tag{29}$$

where $d^h(\mathbf{x}, t)$ is the extended finite element approximation to the damage field. This functional represents an approximation to the total amount of fractured surface area in an arbitrary volume Ω. In a two-dimensional setting, this functional will be referred to as the *crack length functional*.

As a means of identifying when a sharp crack segment should be extended, we monitor the change in this functional. In particular, we consider a small region $\Omega_{t,i}$ centered on each existing sharp crack tip Λ_i. Regions are constructed from the collection of elements within a specified radius, of size R_t, about the sharp crack tip. The radius is chosen to be sufficiently large to roughly encompass the fracture process zone. As a rule of thumb, we have used $R_t \approx 4l$, where l is the regularization length in the phase-field approximation (2). With these definitions in hand, an extension to an existing sharp crack surface is triggered by the quantity $\Delta\Gamma_{l,i}$, where

$$\Delta\Gamma_{l,i}(d^h, t) = \int_{t_0}^{t} \int_{\Omega_{t,i}} \left(\frac{1}{2l}(d^h)^2 + \frac{l}{2}\nabla d^h \cdot \nabla d^h \right) d\mathbf{x}\, dt. \tag{30}$$

In this expression, t is the current time step and t_0 denotes the time of the most recent update to the sharp crack topology. This can be regarded as an estimate to the virtual extension of the fracture surface. The extension of an existing sharp crack tip is considered once $\Delta\Gamma_{l,i} > a_{\min}$, where $a_{\min}$ is a predefined threshold. In practice, we choose $a_{\min} = 3h \sim 4h$ where h denotes the mesh spacing.

4.2 | Crack path definition

The second step in a continuous to discontinuous transition involves addressing the geometrical problem of the sharp crack-path definition. In the spirit of Ziaei-Rad *et al.*[6], in this work the problem of identifying the sharp crack surface from the damage field is addressed using an optimization-based approach.

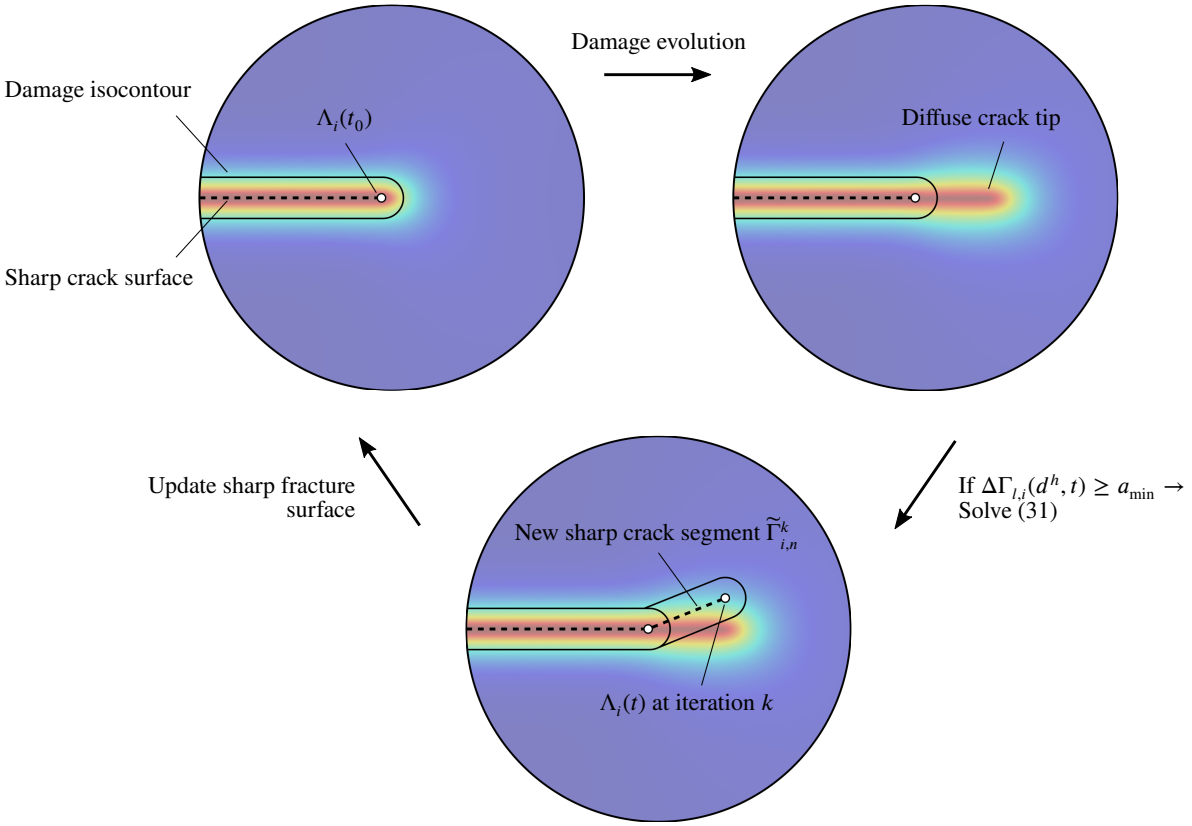

FIGURE 5 Graphical representation of the strategy to facilitate a continuous to discontinuous in the context of phase-field for brittle fracture and a sharp crack tip Λ_i.

The basic idea is as follows. We assume that the sharp crack geometry $\widetilde{\Gamma}$ is composed of a set of connected segments, $\widetilde{\Gamma} = \cup\widetilde{\Gamma}_{i,n}$. Consider the extension of the sharp crack i with crack tip Λ_i by the addition of a new sharp crack segment $\widetilde{\Gamma}_{i,n}$. We associate an auxiliary damage field $d_\Gamma(\mathbf{x})$ with the new segment according to (19). The approach is to identify the length and orientation of the new segment, such that the auxiliary field is as close as possible to the finite element approximation $d^h(\mathbf{x})$ from (28). In other words, we seek to identify the both the length and orientation of a new sharp crack segment such that the functional

$$N_d := \left\| d^h - d_\Gamma \right\|_{L_2(\Omega_{t,i})} \tag{31}$$

is minimized. The search is limited to all straight line segments contained in $\Omega_{t,i}$. We also recall that (31) employs a scaling parameter s that was introduced in (19). This parameter scales the auxiliary damage field such that the sharp crack segments are more effectively placed in a region where the damage approximates unity. Our extensive testing indicates that a value of $s = 2$ results in a robust continuous-discontinuous transition, regardless of the particular problem under consideration.

To minimize the function (31), a direct search method for unconstrained optimization was employed. An initial guess $\widetilde{\Gamma}^0_{i,n}$ for the new sharp crack segment is first introduced, and the algorithm iteratively updates the geometry until the following two criteria are satisfied:

$$\left\| \mathcal{X}\left(\widetilde{\Gamma}^{k+1}_{i,n}\right) - \mathcal{X}\left(\widetilde{\Gamma}^{k}_{i,n}\right) \right\|_2 \leq \mathcal{R}_X \quad \text{and} \quad \left| N_d\left(\widetilde{\Gamma}^{k+1}_{i,n}\right) - N_d\left(\widetilde{\Gamma}^{k}_{i,n}\right) \right| \leq \mathcal{R}_N \tag{32}$$

at which point $\widetilde{\Gamma}_{i,n} = \widetilde{\Gamma}^{k+1}_{i,n}$. Here, $\mathcal{X}(r_{i,n}, \theta_{i,n})$ is the parametrized representation of crack segment $\widetilde{\Gamma}_{i,n}$ (expressed through r and θ as the polar coordinates from sharp crack tip Λ_i), k is the iteration number, $\|\cdot\|_2$ is the ℓ^2-norm, and $\mathcal{R}_X$ and $\mathcal{R}_N$ are the termination tolerances on the argument and objective function value, respectively. In this work, both tolerances are set to $1 \cdot 10^{-7}$.

Algorithm 1 Staggered solution scheme of an optimization-based method for continuous-discontinuous crack propagation in the interval $[t_n, t_{n+1}]$

1: **Initialization** → The displacement, damage and history fields at time t_n are known. Update the prescribed surface tractions $\bar{\mathbf{t}}$ and prescribed displacements $\bar{\mathbf{u}}$ at the current time t_{n+1}.

2: **Compute history** → Calculate the maximum positive energy density obtained in the loading process

$$\mathcal{H} = \begin{cases} W_0^+(\boldsymbol{\varepsilon}_n) & \text{if } W_0^+(\boldsymbol{\varepsilon}_n) > \mathcal{H}_n \\ \mathcal{H}_n & \text{otherwise} \end{cases}$$

and store it as a local history variable at each quadrature point.

3: **Compute damage field** → Compute the damage field by solving the following linear subproblem for d:

$$\frac{\mathcal{G}_c}{l}\left[d - l^2\Delta d\right] - 2(1-d)\mathcal{H} = 0$$

4: **Continuous-discontinuous transition** → Follow the procedure outlined in Algorithm 2.

5: **Compute displacement field** → Compute the displacements for a frozen damage field. Solve

$$\mathrm{Div}\,[\boldsymbol{\sigma}] = \mathbf{0}$$

with the Cauchy stress tensor $\boldsymbol{\sigma}$ given by (26).

Algorithm 2 Algorithmic steps in a continuous to discontinuous transition.

1: **Switching criterion** → Evaluate for every sharp crack tip Λ_i of sharp crack tip set Λ whether the switching criterion is activated.

for $\Lambda_i \in \Lambda$ **do**
  Calculate the virtual crack extension from (30).
  if $\Delta\Gamma_{l,i}(d^h, t) \geq a_{\min}$ **then** $\mathcal{O} \leftarrow \Lambda_i$ ▷ add sharp crack tip to set $\mathcal{O}$
  end if
end for

2: **Crack path definition** → Minimize the objective function

$$N_d := \left\| d^h - d_\Gamma \right\|_{L_2(\Omega_{t,\mathcal{O}})}$$

over a domain $\Omega_{t,\mathcal{O}}$ enclosing all sharp crack tip regions $\Omega_{t,i}$ associated with the sharp crack tips in $\mathcal{O}$.

3: **Enhancement of the kinematics** → Introduce traction-free sharp crack segments in the wake of a diffuse crack tip.

for $e \in \mathcal{E}(e)$ **do** ▷ let $\mathcal{E}$(e) be a finite element discretization
  for $\widetilde{\Gamma}_{i,n} \in \mathcal{O}$ **do**
    if e is split by $\widetilde{\Gamma}_{i,n}$ **then**
      Enhance the element kinematics to represent jump discontinuities (as described in Section 3.2).
    end if
  end for
end for

5 | REPRESENTATIVE NUMERICAL EXAMPLES

We now demonstrate the robustness of the proposed approach for simulating continuous to discontinuous fracture by means of several numerical examples. The proposed multi-field problem is implemented in a staggered solution scheme, as detailed in Algorithms 1 and 2. The former represents a sequence of two subproblems in the pseudo-time interval $[t_n, t_{n+1}]$ for the successive update of the damage field and the displacement field, while the latter summarizes the algorithmic steps in a continuous-to discontinuous transition. The proposed approach for the integrated modeling of continuous-discontinuous crack propagation is summarized in Figure 5 . Accuracy can be ensured by employing sufficiently small load steps.

In the following subsections, we apply our method to several two-dimensional benchmark problems in quasi-static fracture. The computations are performed within the finite element framework using triangular elements under plane strain conditions. A scaling factor of $s = 2$ in (19) and a sharp crack tip region $R_t = 4l$, where l is the regularization length, were used to ensure a robust solution procedure. A relatively large scaling factor ensures that new sharp crack segments are placed in regions where the damage is close to unity. To illustrate the robustness of the method, it will also be shown that the performance of the algorithm is insensitive to changes in the regularization length.

For examples in which the initial crack geometry is known a priori, a two-step process is employed to initialize the discretization. The method described in Borden *et al.*[25] is first used to initialize the tensile strain energy history field in the vicinity of the initial crack. Then, a set of sharp crack segments is placed along the diffuse crack surface, and the kinematics of elements intersected by the segments is enhanced following the procedure described in Section 3.2. In the case when there is no initial crack geometry, the proposed approach requires a special treatment to initialize the optimization-based algorithm. Details regarding this strategy are provided in subsection 5.5.

5.1 | Single edge notched tension test

Consider a square plate with a horizontal notch that is placed at middle height from the left outer surface to the center of the specimen (Figure 6 a). Following Miehe *et al.*[4], the material parameters are set to $\lambda = 121.15$ kN/mm^2, the shear modulus $\mu = 80.77$ kN/mm^2 and the critical energy release rate $\mathcal{G}_c = 2.7$ kN/mm^2. The spatial discretization of the model contains 25,000 elements where the mesh is refined along the expected crack path. The computation is performed in a displacement driven context where the displacement increment is adjusted to $\Delta\bar{u} = 5 \cdot 10^{-6}$ mm upon approaching the peak load. Two different regularization lengths $l_1 = 0.015$ mm and $l_2 = 0.0075$ mm were considered.

The fracture patterns at several loading stages are shown in Figure 7 . The results indicate that the insertion of a discontinuity in the wake of the diffuse crack tip does not inhibit the smooth evolution of the damage field. Figure 8 provides the resulting load-displacement curves, and compares the results to those obtained with a standard phase-field approach (without discontinuity insertion). We note that the changes in the peak load that are observed as a result of the change in the regularization length are

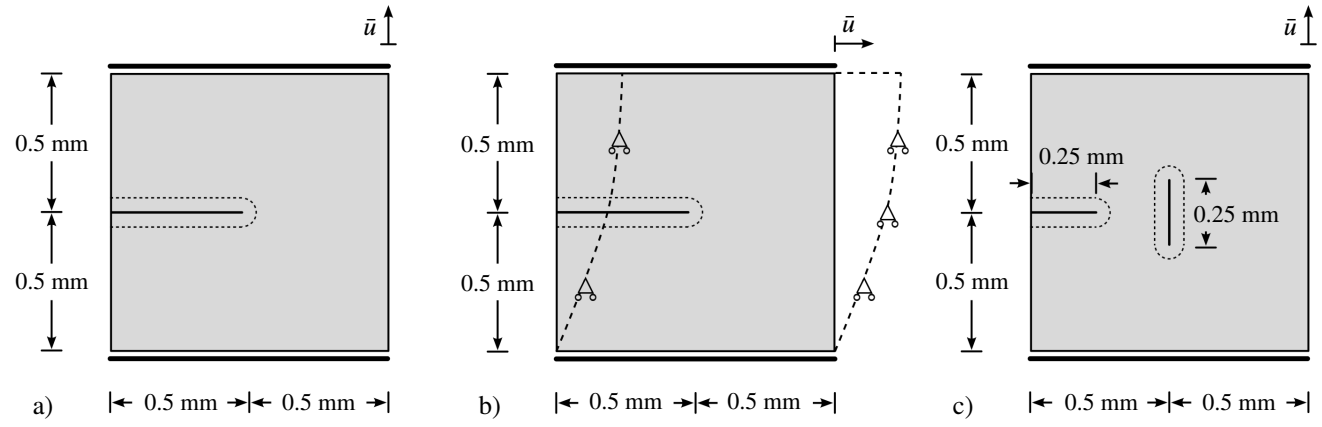

FIGURE 6 Geometry and boundary conditions of a) the single-edge notched tension test b) the single-edge notched shear test and c) the crack coalescence test.

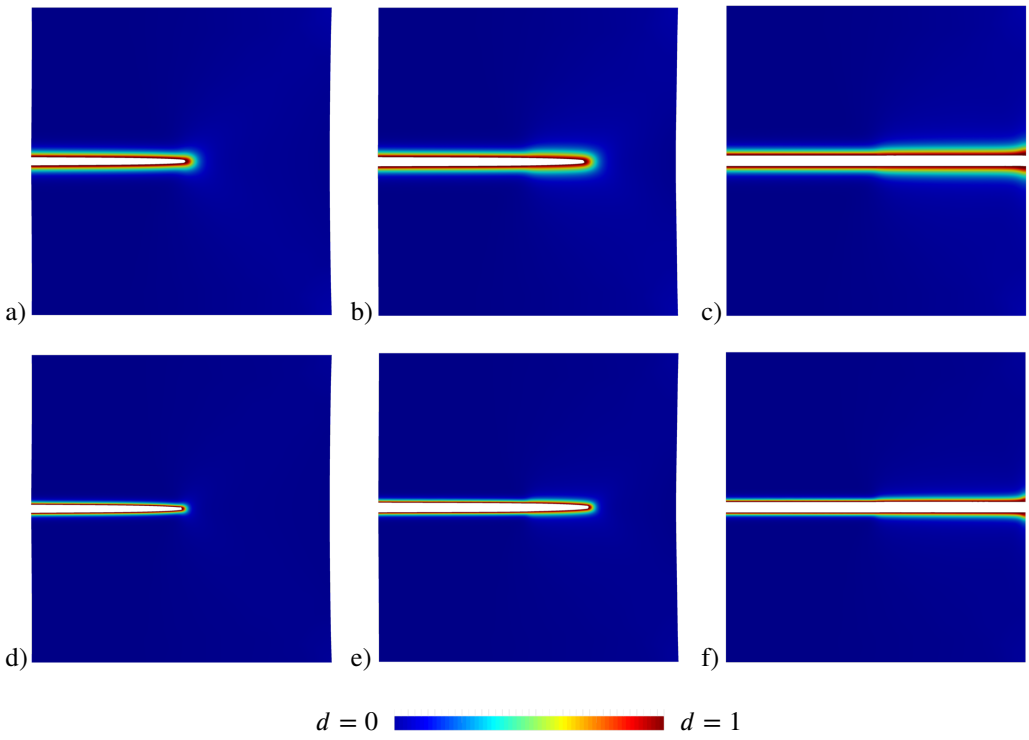

FIGURE 7 Single edge notched test under tension. Damage field at a) $\bar{u} = 5.00 \cdot 10^{-3}$ mm, b) $\bar{u} = 5.65 \cdot 10^{-3}$ mm, c) $\bar{u} = 7.00 \cdot 10^{-3}$ mm for a length scale of $l_1 = 0.015$ mm and at d) $\bar{u} = 5.00 \cdot 10^{-3}$ mm, e) $\bar{u} = 6.05 \cdot 10^{-3}$ mm, f) $\bar{u} = 7.00 \cdot 10^{-3}$ mm for a length scale of $l_1 = 0.0075$ mm. The displacements have been scaled by a factor of 5.

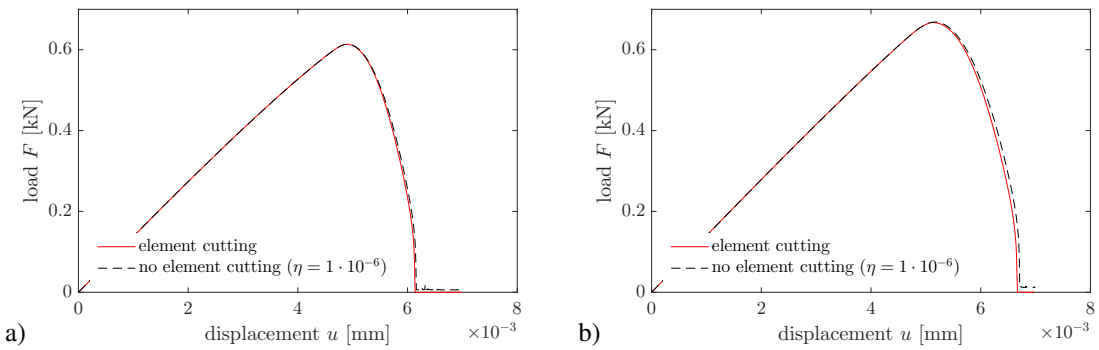

FIGURE 8 Single edge notched test under tension. Load-displacement curves for a) $l_1 = 0.015$ mm and b) $l_2 = 0.0075$ mm.

a feature of this particular phase-field formulation. A decrease of the regularization length leads to an increase of the critical stress, as detailed in Borden *et al.*[25]

With a standard phase-field approach, a regularization parameter η is often employed in the discrete constitutive law for the stress (26) to prevent a loss of ellipticity resulting from fully damaged regions. By contrast, no such parameter is required when discontinuities are inserted in the wake of a propagating sharp crack, and this does improve the accuracy of the results, as described below.

Although the crack pattern and load-displacement curves generally agree well in all cases, the structural response of the current method typically shows a slightly steeper descent of the load in the post-critical regime when compared to the standard

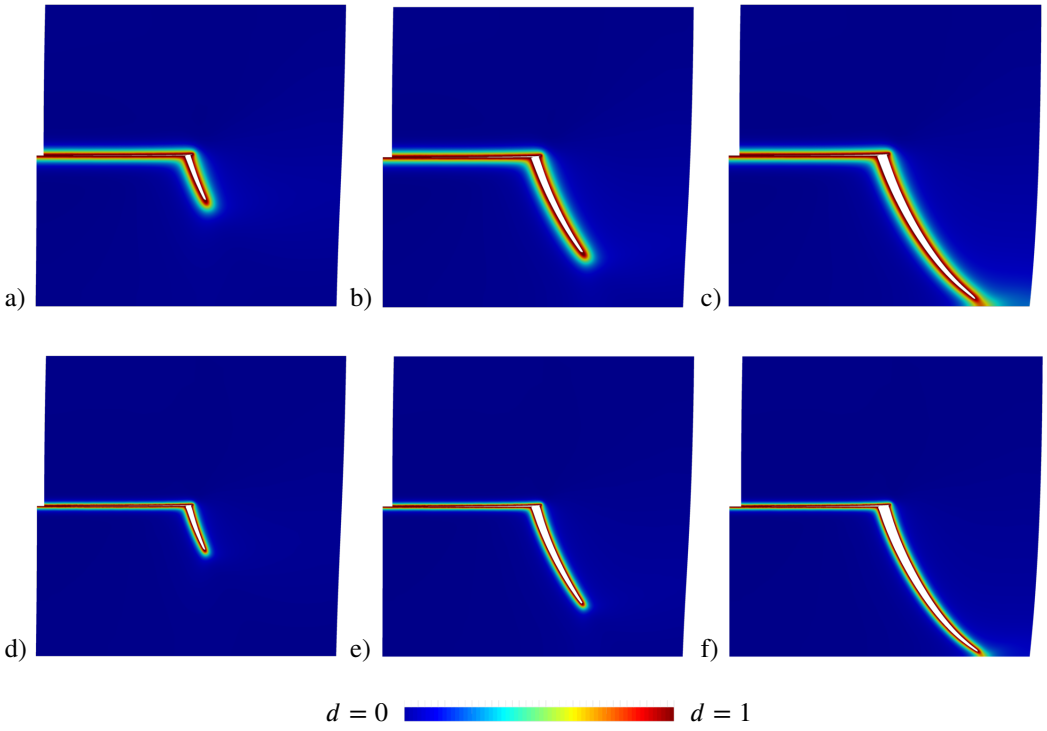

FIGURE 9 Single edge notched test under shear. Damage field at a) $\bar{u} = 1.060 \cdot 10^{-2}$ mm, b) $\bar{u} = 1.180 \cdot 10^{-2}$ mm, c) $\bar{u} = 1.307 \cdot 10^{-2}$ mm for a length scale of $l_1 = 0.015$ mm and at d) $\bar{u} = 1.120 \cdot 10^{-2}$ mm, e) $\bar{u} = 1.270 \cdot 10^{-2}$ mm, f) $\bar{u} = 1.440 \cdot 10^{-2}$ mm for a length scale of $l_1 = 0.0075$ mm. The displacements have been scaled by a factor of 3.

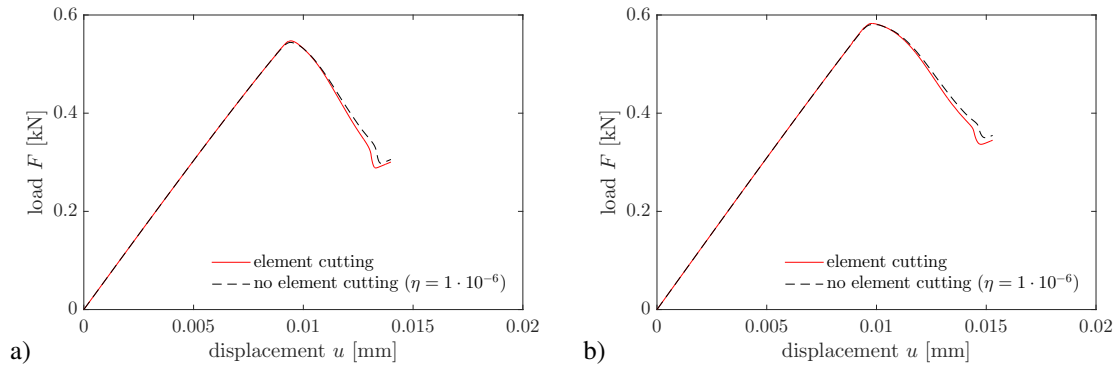

FIGURE 10 Single edge notched test under shear. Load-displacement curves for a) $l_1 = 0.015$ mm and b) $l_2 = 0.0075$ mm.

phase-field results of Miehe *et al.*[3] This originates from the insertion of traction-free crack faces as the sharp crack geometry evolves, which effectively preclude force transmission across the fully damaged region. The results of the proposed approach also indicate a load of exactly zero upon complete fracturing of the specimen, as would be expected. We also note that, compared to classical phase-field and gradient-damage formulations for fracture, the current method appears to exhibit very little widening of the diffuse crack surface as the fracture evolves. This is likely due to both the transition to a fully discontinuous state as well as the lack of any regularization parameter.

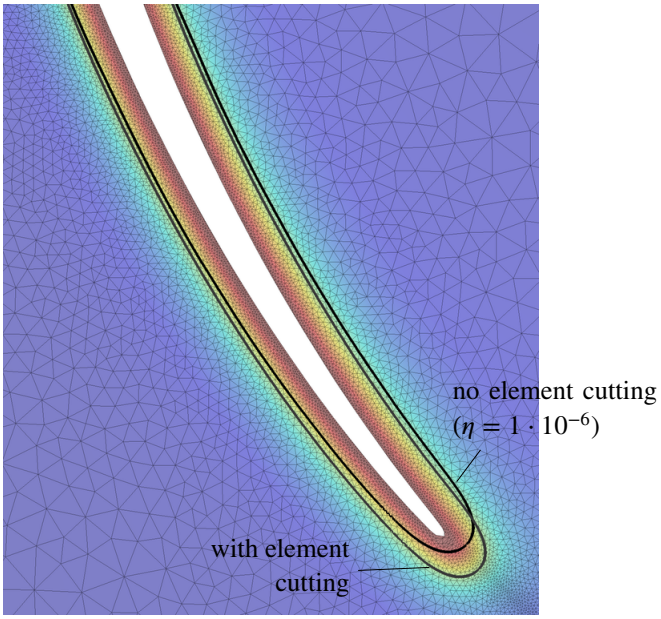

FIGURE 11 Continuous-discontinuous representation of the crack path in the single edge notched shear test at $\bar{u} = 1.24 \cdot 10^{-2}$ mm with regularization length $l = 0.015$ mm. The damage isocontours $d = 0.5$ of the proposed method and the classical phase-field formulation (no element cutting) are compared. The displacements have been scaled by a factor of 3.

5.2 | Single edge notched shear test

The same square plate as in the previous example is now subjected to a shear load. The geometry and boundary conditions are depicted in Figure 6 b. A discretization of 25,000 elements is used with mesh refinement along the expected crack path. Again, we consider two regularization lengths $l_1 = 0.015$ mm and $l_2 = 0.0075$ mm. The computation is performed in a displacement driven context with constant displacement increments of $\Delta\bar{u} = 1 \cdot 10^{-5}$ mm.

The fracture patterns at several loading stages are visualized in Figure 9 and are in excellent agreement with the results reported by Miehe *et al.*[3] The load-displacement curves are depicted in Figure 10 . Similar to the previous example, the proposed method typically predicts a slightly steeper descent of the load in the post-critical regime. A close comparison of damage isocontours (for $d = 0.5$) with and without discontinuity insertion (Figure 11) indicates that the use of the current method has little effect on the damage fields or crack trajectory.

5.3 | Crack coalescence test

To demonstrate the capability of the method to handle topology changes, we now consider an example in which two cracks coalesce. Consider a square plate with two initial cracks, one placed horizontally at middle height from the left outer surface inward, and a second placed vertically in the center of the specimen. The geometry and boundary conditions are illustrated in Figure 6 c. The material parameters are taken to be identical to those used in the single edge-notched tension test example. The discretization is refined along the areas of expected crack propagation, yielding a mesh of 25,000 elements. The computation is performed in a displacement driven context where the displacement increment adjusted to $\Delta\bar{u} = 2.5 \cdot 10^{-6}$ mm upon approaching the peak load.

The results at various stages of loading, for the two different length scales under consideration, are given in Figure 12 . The corresponding load-displacement curves are given in Figure 13 . The proposed method is clearly capable of modeling the merge of the two continuous-discontinuous cracks.

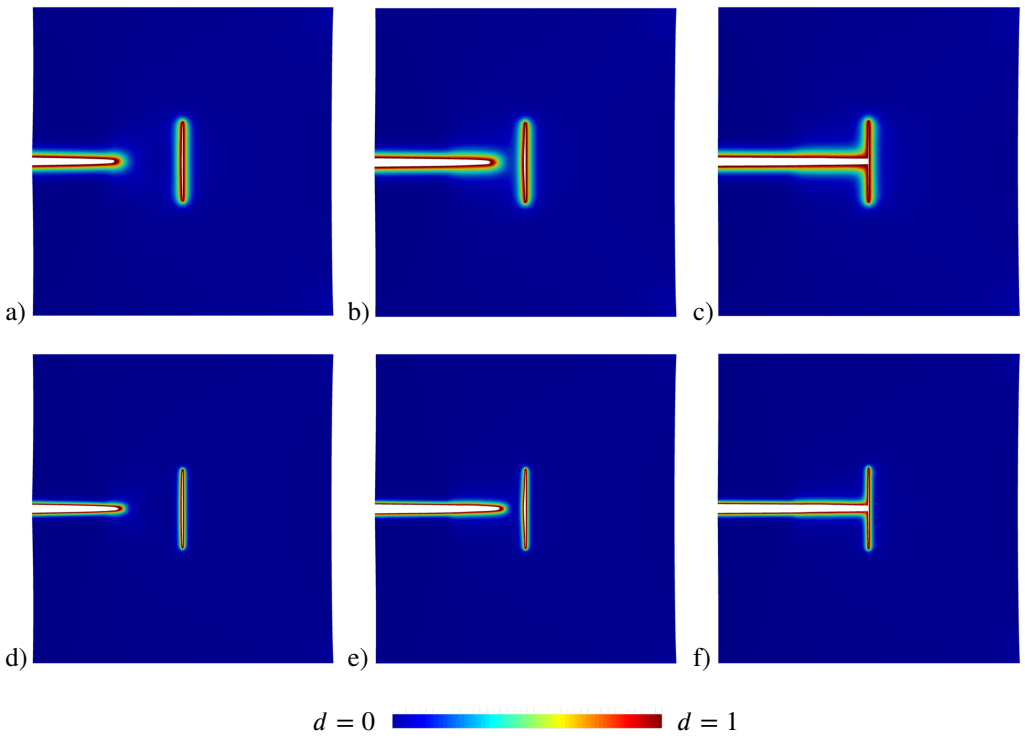

FIGURE 12 Damage field for the crack coalescence test at a) $\bar{u} = 4.85 \cdot 10^{-3}$ mm, b) $\bar{u} = 4.98 \cdot 10^{-3}$ mm, c) $\bar{u} = 5.05 \cdot 10^{-3}$ mm for a length scale of $l_1 = 0.015$ mm and at d) $\bar{u} = 5.15 \cdot 10^{-3}$ mm, e) $\bar{u} = 5.33 \cdot 10^{-3}$ mm, f) $\bar{u} = 5.45 \cdot 10^{-3}$ mm for a length scale of $l_1 = 0.0075$ mm. The displacements have been scaled by a factor of 5.

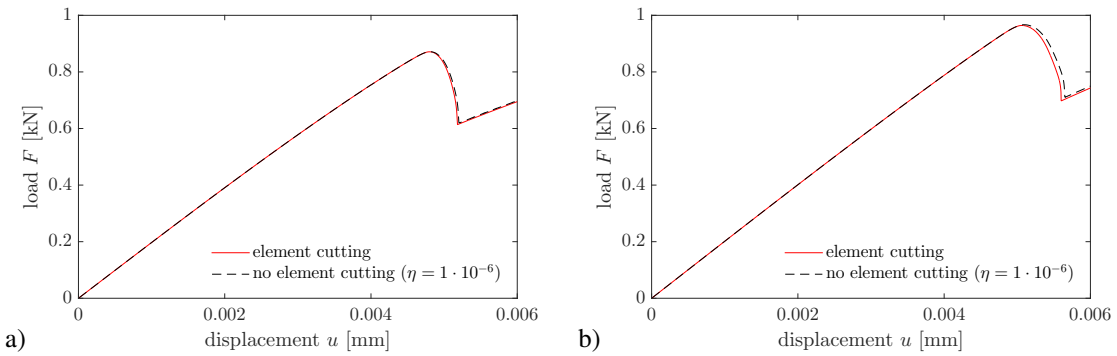

FIGURE 13 Load-displacement curves for the crack coalescence test for a) $l_1 = 0.015$ mm and b) $l_2 = 0.0075$ mm.

5.4 | Notched bimaterial tension test

We now consider a problem in which a propagating crack is expected to bifurcate, or split into two separate cracks. Such problems are challenging because they represent a dramatic change in the crack topology. In this example, we modify the current method to accommodate such a possibility. In particular, we use an initial guess of two new sharp crack segments that could be different at the conclusion of the optimization algorithm. The optimization algorithm attempts to place both new sharp crack segments within the damage pattern that has formed ahead of the current sharp crack tip. If the two segments are placed at an angle between them that is above a threshold θ_c, then the algorithm assumes that a bifurcation has occurred and both segments are

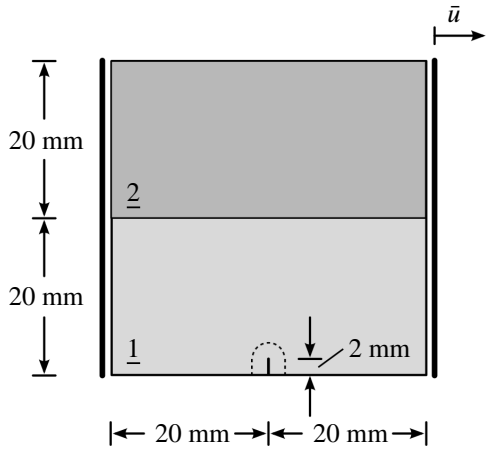

FIGURE 14 Geometry and boundary conditions for the notched bimaterial tension test from Moës *et al.*[5]

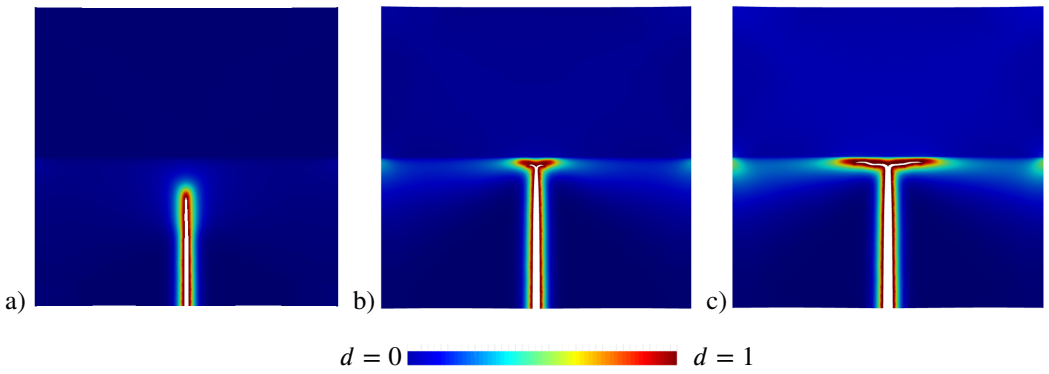

FIGURE 15 Notched bimaterial specimen under tension. Damage field at a) $\bar{u} = 7.51 \cdot 10^{-3}$ mm, b) $\bar{u} = 1.16 \cdot 10^{-2}$ mm, c) $\bar{u} = 1.43 \cdot 10^{-2}$ mm. The displacements have been scaled by a factor of 2.

added as extensions to the existing sharp crack tip. Conversely, if the two segments are separated by an angle below θ_c, then the segments are collapsed into a single one and the process repeats.

We apply this approach to the bimaterial tension test from Moës *et al.*[5] Consider a plate made of two materials with a notch of length $L = 2.0$ mm at the center of the bottom edge. The geometry and boundary conditions are shown in Figure 14 . The material parameters are assumed to be $\lambda_1 = 10.47 \cdot 10^3$ kN/mm^2, $\lambda_2 = 10\lambda_1$, $\mu_1 = 15.71 \cdot 10^3$ kN/mm^2, $\mu_2 = 10\mu_1$, $\mathcal{G}_{c,1} = 1 \cdot 10^{-3}$ kN/mm and $\mathcal{G}_{c,2} = 10\mathcal{G}_{c,1}$ for the bulk moduli, shear moduli, and critical energy release rates, respectively. The index refers to the top and bottom materials. The spatial discretization of the model contains 15,000 elements with a mesh that is refined along the assumed crack path.

The computation is performed in a displacement driven context where the initial displacement increment is $\Delta\bar{u} = 10^{-4}$ mm, which is adjusted to $\Delta\bar{u} = 10^{-5}$ mm when the crack approaches the bimaterial interface. The critical bifurcation angle was set to $\theta_c = 30°$. The fracture patterns at several loading stages are shown in Figure 15 . The crack propagates as a single, connected curve until it approaches the bimaterial interface. The crack then bifurcates into two distinct branches, as branching requires less energy than continuing into the upper material.

5.5 | L-shaped panel test

Another commonly studied problem is the L-shaped panel test. The geometry for the problem and the boundary conditions are illustrated in Figure 16 . Following Ambati *et al.*[30], the material parameters are $\lambda = 6.16$ kN/mm^2, $\mu = 10.95$ kN/mm^2 and $\mathcal{G}_c = 8.9 \cdot 10^{-5}$ kN/mm^2. The regularization length is chosen be $l = 2.5$ mm. The spatial discretization of the model contains

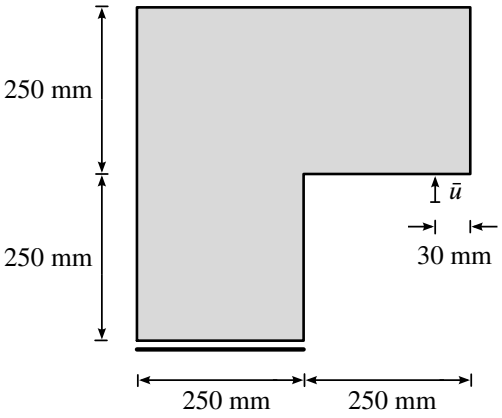

FIGURE 16 Geometry and boundary conditions of the L-shaped panel test.

22,000 elements and is refined along the predicted crack path. The computation is performed in a displacement driven context with constant displacement increments of $\Delta\bar{u} = 10^{-3}$ mm.

As the geometry does not contain an initial crack, the optimization process is initiated as soon as the damage reaches a critical value of $d \geq 0.95$. The first instance of the optimization algorithm optimizes for an entire sharp crack segment, rather than merely optimizing for the new sharp crack tip. This small extension to the main algorithm permits us to study these kind of crack nucleation problems in a straightforward manner.

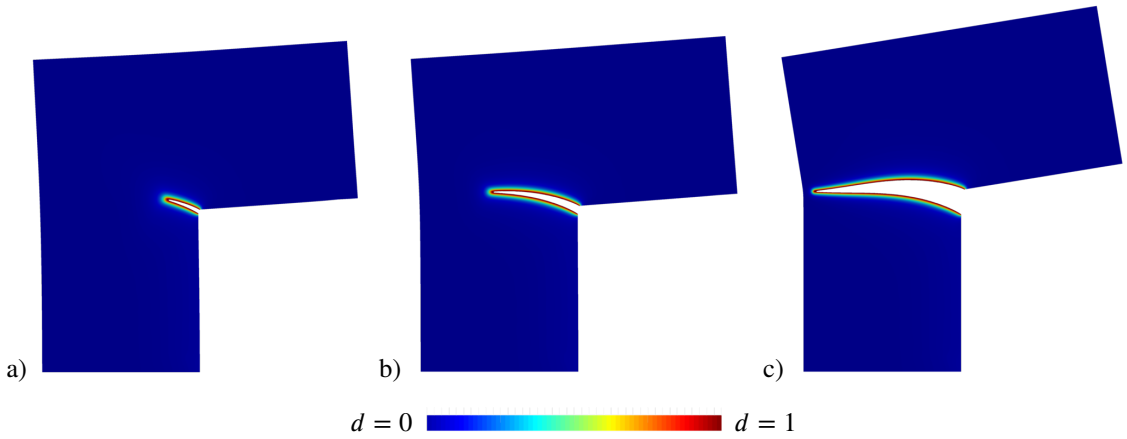

FIGURE 17 Damage field at a) $\bar{u} = 0.32$ mm, b) $\bar{u} = 0.40$ mm, c) $\bar{u} = 1.0$ mm for the L-shaped panel using a length scale of $l = 2.5$ mm. The displacements have been scaled by a factor of 75.

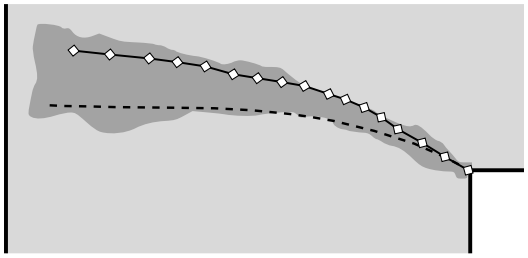

FIGURE 18 Proposed method (dashed line) and the results from Ferté *et al.*[31] (solid line) compared to experimentally observed crack patterns from Winkler[32] (shaded area).

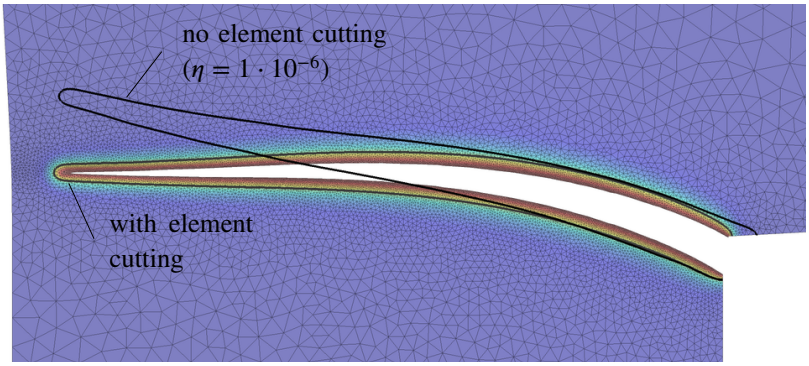

FIGURE 19 Comparison between the proposed method and the classical phase-field formulation using a damage isocontour of $d = 0.5$. The displacements have been scaled by a factor of 25.

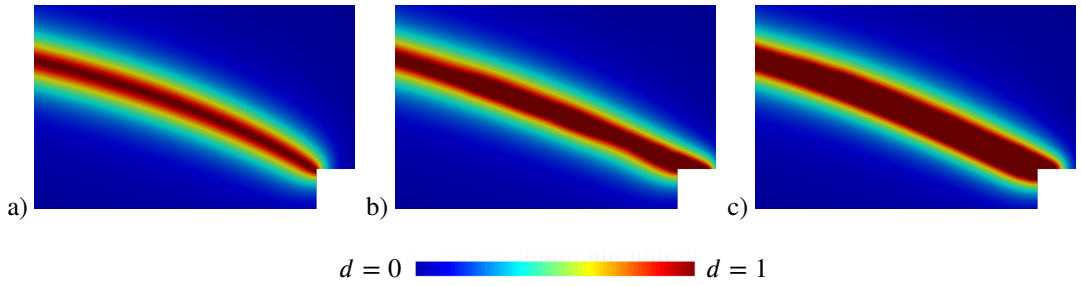

FIGURE 20 Widening at the base of the crack at $\bar{u} = 1.0$ mm for different values of η. a) the proposed continuous-discontinuous method with $\eta = 0$, b) classical phase-field with $\eta = 10^{-6}$, c) classical phase-field with $\eta = 10^{-4}$.

Figure 17 depicts the damage field at several stages of loading. Figure 18 shows that the sharp crack trajectory retrieved by the proposed method falls within the range of experimental observations. In addition, it agrees qualitatively with results obtained by alternative computational methods such as the cohesive zone approach from Ferté *et al.*[31] Somewhat surprisingly, the classical phase-field formulation from Miehe *et al.*[3] (without cutting) predicts crack growth along a different trajectory, as seen in Figure 19 . The reason for this behavior was already briefly introduced in the first numerical example. In the case of a nonzero value for η, spurious tractions across the fracture surface adversely affect the damage evolution, effectively widening the regularized crack surface. This effect is amplified for increasing η in the presence of relatively large strains, as is the case at the base of the crack in the L-shaped panel. In strong contrast, the proposed method introduces traction-free sharp cracks in the wake of the diffuse crack tip, effectively preventing tractions from being transmitted across the fully damaged zone. This results in a regularized fracture surface of constant width along the crack path and a more realistic structural response. Figure 20 provides an illustration of this issue.

5.6 | Notched plate with an off-center hole

Consider the example described by Ambati *et al.*[30] of a notched plate with a load applied to a top pin and a fully fixed bottom pin. In addition, there is an off-center hole in the specimen that induces mixed-mode fracture. The geometry and boundary conditions are shown in Figure 21 a. The specimen material is a cement mortar that is modeled by choosing the material parameters $\lambda = 1.95$ kN/mm^2, $\mu = 2.45$ kN/mm^2 and $\mathcal{G}_c = 2.28 \cdot 10^{-3}$ kN/mm. The regularization length is chosen to be $l = 0.4$ mm. The numerical simulation is performed using fixed displacement increments of $\Delta\bar{u} = 1 \cdot 10^{-3}$ mm. A discretization consisting of 35,000 triangular elements is used, refined in areas where the crack is expected to propagate.

Figure 22 shows the crack patterns at several stages of loading. A curved crack develops from the notch to the large hole. Later, a secondary crack appears from the right edge of the hole to the outer edge of the sample. The fracture pattern corresponds

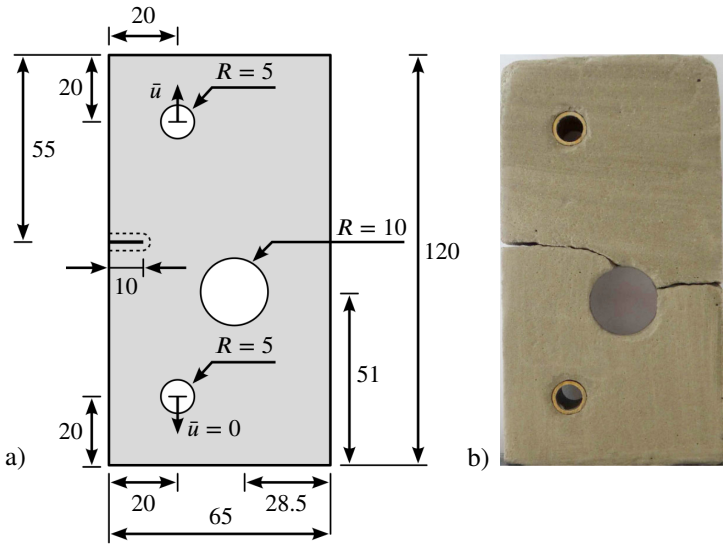

FIGURE 21 Notched plate with an off-center hole. a) Geometry and boundary conditions. All dimensions are in millimeters. b) Crack path of a fully fractured specimen from Ambati *et al.*[30]

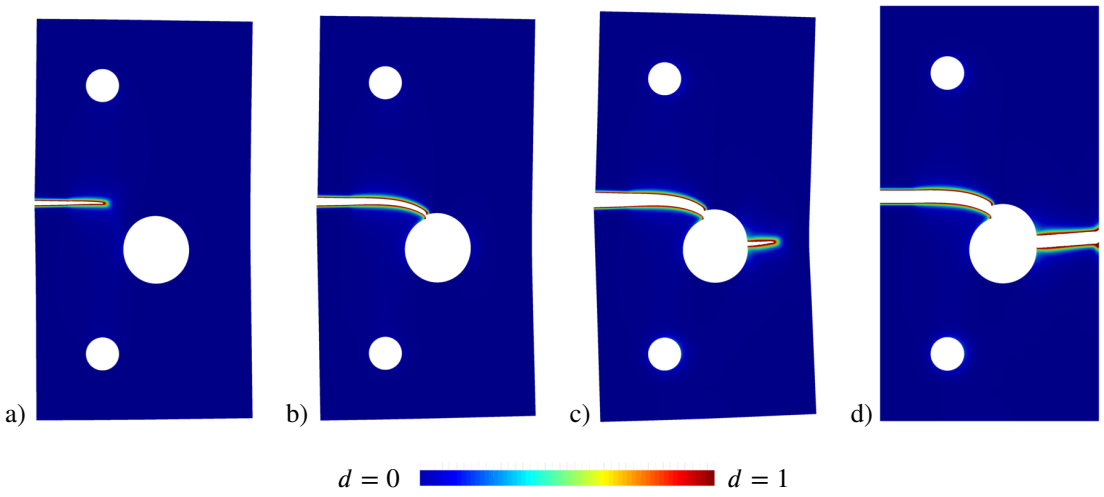

FIGURE 22 Notched plate with hole. Damage field at a) $\bar{u} = 0.360$ mm, b) $\bar{u} = 0.580$ mm, c) $\bar{u} = 1.137$ mm and d) $\bar{u} = 1.217$ mm. The displacements have been scaled by a factor of 3.

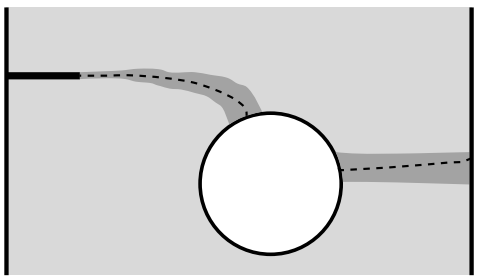

FIGURE 23 The calculated sharp crack path (dashed line) and the experimental range (shaded area) for the notched plate with an off-center hole.

well to the experimentally observed crack pattern, see Figure 21 b, and to the numerical results from Ambati *et al.*[30] Moreover, Figure 23 illustrates the extent to which the simulated crack path falls within the window of experimental observations.

6 | CONCLUSIONS

In this work, an integrated approach was outlined for the coupling of a phase-field formulation to a more traditional description of fracture, based on the extended finite element method. The following three aspects were central to the method: (i) The use of the crack length functional inside a sharp crack tip region was proposed to provide a quantitative measure on when to initiate a continuous-discontinuous transition. (ii) The crack path definition was addressed through an optimization problem. A sharp crack geometry can be retrieved by finding the auxiliary damage field $d_\Gamma(\mathbf{x}, \Gamma)$ that is closest to the true damage field $d^h(\mathbf{x})$, stemming from the phase-field framework. This strategy leads to a robust computational scheme for the simulation of multi-crack propagation. (iii) The proposed framework was shown to systematically place traction-free sharp cracks in the wake of a diffuse crack tip, where the damage is equal or close to one. This eliminates the need for a regularization parameter that classical phase-field methods employ to circumvent a potential loss in ellipticity in fully damaged regions.

A transition from damage to fracture was constructed through the use of the extended finite element method as the enabling technology. The material regions approach builds on this concept by providing a systematic way to deal with the kinematics of complex fracture networks. By defining minor extensions, the capability of the method to handle initiation, growth, branching and coalescence of cracks was demonstrated.

This manuscript gives rise to several areas for future investigation. First and foremost, we mention the extension of some of the basic elements to three-dimensional problems. Such an extension is expected to be non-trivial, with particular regard to the geometric representation of the sharp crack geometry. We also note that while the current approach does rely on the phase-field method to drive the evolution of the crack geometry, it may not be necessary to maintain the phase-field in regions where the discontinuity surface has been inserted. The insertion of the sharp crack geometry and accompanying X-FEM enrichment provides the ability to represent the crack opening, and as such, the damaged zone on either side of the crack surface stemming from the original phase field may not need to be maintained. Finally, the transition to a sharp fracture surface with X-FEM enrichment may facilitate adaptivity in the sense of coarsening the mesh in the wake of the evolving crack front.

Acknowledgements

This work was performed under a research project from Sandia National Laboratories. The support to Duke University is gratefully acknowledged.

References

1. G.A. Francfort, J.-J. Marigo. Revisiting brittle fracture as an energy minimization problem. *Journal of the Mechanics and Physics of Solids.* 1998;46(8):1319 - 1342.

2. B. Bourdin, G.A. Francfort, J.-J. Marigo. Numerical experiments in revisited brittle fracture. *Journal of the Mechanics and Physics of Solids.* 2000;48(4):797–826.

3. C. Miehe, M. Hofacker, F. Welschinger. A phase field model for rate-independent crack propagation: Robust algorithmic implementation based on operator splits. *Computer Methods in Applied Mechanics and Engineering.* 2010;199(45-48):2765 - 2778.

4. C. Miehe, F. Welschinger, M. Hofacker. Thermodynamically consistent phase-field models of fracture: Variational principles and multi-field FE implementations. *International Journal for Numerical Methods in Engineering.* 2010;83(10):1273–1311.

5. N. Moës, C. Stolz, P.-E. Bernard, N. Chevaugeon. A level set based model for damage growth: The thick level set approach. *International Journal for Numerical Methods in Engineering.* 2011;86(3):358–380.

6. V. Ziaei-Rad, L. Shen, J. Jiang, Y. Shen. Identifying the crack path for the phase field approach to fracture with non-maximum suppression. *Computer Methods in Applied Mechanics and Engineering.* 2016;312:304–321.

7. N. Sukumar, J.E. Dolbow, N. Moës. Extended finite element method in computational fracture mechanics: a retrospective examination. *International Journal of Fracture.* 2015;196(1-2):189–206.

8. L. Ambrosio, V.M. Tortorelli. Approximation of functional depending on jumps by elliptic functional via Γ-convergence. *Communications on Pure and Applied Mathematics.* 1990;43(8):999–1036.

9. D. Mumford, J. Shah. Optimal approximations by piecewise smooth functions and associated variational problems. *Communications on pure and applied mathematics.* 1989;42(5):577–685.

10. R. de Borst, C.V. Verhoosel. Gradient damage vs phase-field approaches for fracture: Similarities and differences. *Computer Methods in Applied Mechanics and Engineering.* 2016;312:78 - 94. Phase Field Approaches to Fracture.

11. J. Mazars, G. Pijaudier-Cabot. From damage to fracture mechanics and conversely: A combined approach. *International Journal of Solids and Structures.* 1996;33(20):3327 - 3342.

12. J. Oliver, M. Cervera, O. Manzoli. Strong discontinuities and continuum plasticity models: the strong discontinuity approach. *International Journal of Plasticity.* 1999;15(3):319 - 351.

13. J. Oliver, A.E. Huespe, M.D.G. Pulido, E. Chaves. From continuum mechanics to fracture mechanics: the strong discontinuity approach. *Engineering Fracture Mechanics.* 2002;69(2):113 - 136.

14. J. Oliver, A.E. Huespe, M.D.G. Pulido, E. Samaniego. On the strong discontinuity approach in finite deformation settings. *International Journal for Numerical Methods in Engineering.* 2003;56(7):1051–1082.

15. M. Jirasek, T. Zimmermann. Embedded crack model. Part II: Combination with smeared cracks. *International Journal for Numerical Methods in Engineering.* 2001;50(6):1291–1305.

16. C. Comi, S. Mariani, U. Perego. An extended FE strategy for transition from continuum damage to mode I cohesive crack propagation. *International Journal for Numerical and Analytical Methods in Geomechanics.* 2007;31(2):213–238.

17. F. Cazes, M. Coret, A. Combescure, A. Gravouil. A thermodynamic method for the construction of a cohesive law from a nonlocal damage model. *International Journal of Solids and Structures.* 2009;46(6):1476 - 1490.

18. S. Cuvilliez, F. Feyel, E. Lorentz, S. Michel-Ponnelle. A finite element approach coupling a continuous gradient damage model and a cohesive zone model within the framework of quasi-brittle failure. *Computer Methods in Applied Mechanics and Engineering.* 2012;237:244 - 259.

19. F. Cazes, A. Simatos, M. Coret, A. Combescure. A cohesive zone model which is energetically equivalent to a gradient-enhanced coupled damage-plasticity model. *European Journal of Mechanics - A/Solids.* 2010;29(6):976 - 989.

20. F. Dufour, G. Pijaudier-Cabot, M. Choinska, A. Huerta. Extraction of a crack opening from a continuous approach using regularized damage models. *Computers & Concrete.* 2008;5(4):375–388.

21. F. Dufour, G. Legrain, G. Pijaudier-Cabot, A. Huerta. Estimation of crack opening from a two-dimensional continuum-based finite element computation. *International Journal for Numerical and Analytical Methods in Geomechanics.* 2012;36(16):1813–1830.

22. E. Tamayo-Mas, A. Rodríguez-Ferran. A medial-axis-based model for propagating cracks in a regularised bulk. *International Journal for Numerical Methods in Engineering.* 2015;101(7):489–520.

23. Y. Wang, H. Waisman. From diffuse damage to sharp cohesive cracks: A coupled XFEM framework for failure analysis of quasi-brittle materials. *Computer Methods in Applied Mechanics and Engineering.* 2016;299:57 - 89.

24. B. Giovanardi, A. Scotti, L. Formaggia. A hybrid XFEM-Phase field (Xfield) method for crack propagation in brittle elastic materials. *Computer Methods in Applied Mechanics and Engineering.* 2017;320:396 - 420.

25. M.J. Borden, C.V. Verhoosel, M.A. Scott, T.J.R. Hughes, C.M. Landis. A phase-field description of dynamic brittle fracture. *Computer Methods in Applied Mechanics and Engineering.* 2012;217:77–95.

26. I. Babuška, M.B. Rosenzweig. A finite element scheme for domains with corners. *Numerische Mathematik.* 1972;20(1):1–21.

27. P. Grisvard. *Elliptic Problems in Nonsmooth Domains*. Society for Industrial and Applied Mathematics; 2011.

28. N. Moës, J.E. Dolbow, T. Belytschko. A finite element method for crack growth without remeshing. *International Journal for Numerical Methods in Engineering.* 1999;46(1):131–150.

29. C.L. Richardson, J. Hegemann, E. Sifakis, J. Hellrung, J.M. Teran. An XFEM method for modeling geometrically elaborate crack propagation in brittle materials. *International Journal for Numerical Methods in Engineering.* 2011;88(10):1042–1065.

30. M. Ambati, T. Gerasimov, L. De Lorenzis. A review on phase-field models of brittle fracture and a new fast hybrid formulation. *Computational Mechanics.* 2015;55(2):383–405.

31. G. Ferté, P. Massin, N. Moës. 3D crack propagation with cohesive elements in the extended finite element method. *Computer Methods in Applied Mechanics and Engineering.* 2016;300:347–374.

32. B.J. Winkler. *Traglastuntersuchungen von unbewehrten und bewehrten Betonstrukturen auf der Grundlage eines objektiven Werkstoffgesetzes für Beton*. Innsbruck University Press; 2001.